Construction and Building Materials 344 (2022) 128293

Contents lists available at ScienceDirect

Construction and Building Materials

journal homepage: www.elsevier.com/locate/conbuildmat

Effective medium electrical response model of carbon nanotubes cement-based composites

Daniel A. Triana-Camacho [a], David A. Miranda [a], Enrique García-Macías [b,*], Oscar A. Mendoza Reales [c], Jorge H. Quintero-Orozco [a]

[a] Escuela de Física, Universidad Industrial de Santander, Cra 27 Calle 9 Bucaramanga, Colombia
[b] Escuela Técnica Superior de Ingeniería de Caminos, Canales y Puertos, Universidad de Granada, Campus Universitario de Fuentenueva, Granada 18071, Spain
[c] Universidade Federal do Rio de Janeiro, Av. Pedro Calmon 550 Cidade Universitária, Rio de Janeiro, 21941-901, Brazil

ARTICLE INFO

Keywords:
Carbon nanotubes
Cement
Circuital model
Dispersant agents
Effective-medium theory
Impedance spectroscopy

ABSTRACT

The electrical properties of carbon nanotubes (CNT) cement-based composites have been modeled in previous works by circuit models or homogenization theories. An alternative approach is the use of an effective medium theory with induced polarization: In this work, a new model based on the generalized effective medium theory of induced polarization (GEMTIP) with cylindrical inclusions is proposed. The presented results and discussion show its applicability to interpret the electrical impedance spectra of cylindrical cement samples doped with multi-walled CNTs (MWCNTs). The MWCNTs were dispersed in different media: one nonionic surfactant, two superplasticizers, a cationic type polycarboxylate ether, and an anionic type naphthalene sulfonate. Particle dispersion and their sizes were analyzed by Ultraviolet–Visible (UV–Vis) spectroscopy, and Scanning Electron Microscopy (SEM) measurements. Two electrode electrical impedance spectra were measured and analyzed by circuital models and the proposed GEMTIP model. The results demonstrate the efficiency of the proposed model in describing the Alternating Current (AC) response of cement/CNT composites irrespective of the dispersant agent used to elaborate the samples.

1. Introduction

The importance of cement as a building material has constantly motivated research to understand and improve its physical and chemical properties. Cement-based matrices have a highly heterogeneous microstructure, which has a preponderant role in its macroscopic performance and is originated by an exothermic hydration process [1]. The addition of fillers to cement is a common practice to improve its properties; additives such as microparticles and nanoparticles have shown improvements in the thermodynamic, rheological, electric, and piezoelectric properties of cement pastes, mortars, and concretes [2]. Nanoclays, iron, aluminum, silicon, titanium oxides, zeolites, graphene, nanofibers, and carbon nanotubes (CNTs) have been found to improve the physical properties of cement-based composites [3], including water absorption reduction [4,5], increased workability, lower pressure on the formwork, higher fracture toughness, reduced setting time, accelerated hydration reaction [6], and increased ultimate strength [7]. Additionally, an increase in the piezoelectric properties of cement-based composites has been observed with the addition of nanomaterials such as CNTs, some oxides (TiO_2, ZnO_2, SiO_2), and other ceramics such as lead zirconate titanate (PZT) [8].

Another piezoelectric property is the piezoresistivity; therefore, a reduction of this property has been reported when doped with CNTs at volume fractions under the percolation threshold (<1%) [9]. While other reports found an increment in the effective piezoresistivity of 20% if the CNTs volume fraction is 0.2% [10]; however, Wen and Chung argued there are other involving variables that also affect the piezoelectric response, such as CNTs size [11]. Due to their high aspect ratio (~100–1000), CNTs have been found able to increase the mechanical strength of cement-based composites by improving the bonding forces between hydration products [12]. In addition, due to their electrical properties such as conductivity ($\sigma = 10^{-4}$ Ω cm), CNTs have been also used for creation of self-diagnosis composites in smart structures [13].

Three charge transport mechanisms dominate the electrical properties of cement-based composites filled with CNTs: (i) the displacement currents through the cement matrix, that depends on the electrical permittivity of the matrix material; (ii) the formation of conductive paths between adjacent CNTs; (iii) electron hopping between separated CNTs. Mechanisms (ii) and (iii) strongly depend on the concentration of CNTs in the cement matrix [14,15]. Low concentrations of CNTs can substantially decrease the Direct Current (DC) resistance [16].

* Corresponding author.
E-mail addresses: dantrica@saber.uis.edu.co (D.A. Triana-Camacho), enriquegm@ugr.es (E. García-Macías).

https://doi.org/10.1016/j.conbuildmat.2022.128293
Received 1 April 2022; Received in revised form 20 June 2022; Accepted 28 June 2022
Available online 4 July 2022

However, changes in the electric properties of CNTs-based cementitious composites strongly depend on the hydration degree of the sample [17], the water/cement ratio [18], the volume fraction of CNTs [19], and the dispersing agents used in the dispersion [20–22].

One commonly used strategy to disperse CNTs into a cement matrix is the use of surfactants as dispersing agents [23–25]. Products such as Triton TX-100, which is a nonionic surfactant, produce many bubbles when mixed with cement paste [26] and induce a large number of spherical macropores in the cured material. These macropores reduce the density of cement-based composites, affecting their mechanic and electric properties [21]. Other products, such as ether polycarboxylate and naphthalene sulphonate, which are commercial superplasticizers for concrete, can also act as dispersing agents for CNTs. It has been observed that naphthalene sulphonates achieve better dispersion efficiency and reach higher conductivity values in DC when compared with ether polycarboxylates [27].

The effect of dispersing agents on cement properties has been studied by electrical impedance measurements and circuital models [27,28], being the lumped circuit for CNTs/cement composites proposed by Dong the most popular one [29]. The advantages of Alternating Current (AC) electrical techniques to characterize cement-based composites include (i) the relaxation times at high frequency and their possible relationship with the porous structure of cement can be determined [30], making pore size distributions accessible [31]; (ii) the dispersion quality of CNTs into the cement matrix can be characterized; and (iii) physical and chemical properties, such as hydration degree, flexural strength, and compressive modulus, can be estimated by taking into account the electric charge transference [32–34].

Even though the circuital models allow the analysis of the physical properties of cement-based composites by electrical measurements, their application is limited by the number of passive elements and how they are interconnected. Mean Field Homogenization (MFH) constitutes another popular approach to predict the physical properties of CNT-based composites. Originally, MFH was developed by Eshelby in 1957 to study the elastic properties of composite materials doped with dilute concentrations of ellipsoidal particles [35]. Mori–Tanaka extended in 1973 the original theory by Eshelby to model non-dilute filler concentrations. This approach allows one to account for the filler orientation distribution through suitable probability density functions [36]. MFH has also been applied to scale the thermal properties of the different phases of the calcium silicate hydrate (C-S-H) structure [37], and to estimate the electrical conductivity in DC of CNT-based composites [14]. Furthermore, there is the Generalized Effective-Medium Theory of Induced Polarization (GEMTIP), which takes the same principles from MFH. This theory allows calculating the AC conductivity and resistivity of a material that includes dispersed phases [38]. GEMTIP was initially developed to describe the electric properties of rocks with spherical and elliptical inclusions; although, its use has been extended in recent years to other applications such as the modeling of normal and abnormal biological tissue [39,40].

In this work, a model with cylindrical inclusions based on the GEMTIP theory is proposed to interpret experimental data obtained from CNT-cement-based composites. The presented model accounts for cylindrical inclusions based on the GEMTIP theory and allows to interpret experimental data obtained from CNT-cement-based composites. The advantages of creating models based on GEMTIP are the possibility to obtain, by fitting experimental data, the model parameters associated with physical properties of the modeled material, independent of the characteristics of a circuital element. Compared with the existing literature, the main innovations in this paper comprise: (i) Development of a novel physically-based micromechanics model and benchmarking against an enhanced version of the circuital model proposed by Dong et al. [29]; (ii) Experimental and theoretical characterization of the AC electric and physico-chemical properties of CNTs dispersed in three different dispersant agents; (iii) Use of the developed GEMTIP model to infer material microscopical parameters not achievable with circuital models, including the polarizability constants of CNTs and pores, as well as the volume fraction of pores. In addition, parameter estimation represents an essential aspect in designing and optimizing of new advanced materials such as cement/CNT composites. Hence, the number of iterations, ill-conditioning, and the lack of convergence in the inverse calibration of the GEMTIP model have been minimized by fixing the parameters determined in the experimental campaign. The circuital model in (i) represents another innovative aspect of the present work, which replaces the Warburg element commonly used in the literature with a constant phase element. The comparison of this model against experimental data demonstrates the ability of this new element to reproduce the electrical impedance spectra at low frequencies for a wide variety of dispersant agents used in the mixture. The remainder of this manuscript is organized as follows. Section 2 (methods) contains the materials, experimental setup, and techniques performed to determine the physical properties and model electrical behavior in AC of MWCTs-based composites. Section 3 (results) shows how it gets the best configuration of dispersants, the physical parameters of composites, an alternative lumped circuit model, the mathematical construction and fitting of the GEMTIP model for cylindrical inclusions. Finally, Section 4 concludes the paper.

Table 1
Properties of multi-wall carbon nanotubes produced via catalytic chemical vapor deposition (CCVD).

Average diameter [nm]	Average length [μm]	Carbon purity [%]	Transition metal oxide [%]	Surface area [m^2/g]	Volume resistivity [Ω cm]
9.5	1.5	90	<1	250–300	10^{-4}

2. Methods

2.1. Materials

The materials used in this work were (i) standard portland cement produced by Argos, Colombia, under Colombian standard NTC121 (equivalent to ASTM C1157). (ii) A nonionic surfactant (Triton TX-100) [41]. (iii) A cationic superplasticizer (SikaPlast-328) [42], which is polycarboxylate ether-based, produced under the ASTM C-494 standard. (iv) An anionic superplasticizer (EUCON 37) [43], which is naphthalene sulphonate based. And (v) multi-walled carbon nanotubes (MWCT) reference NC7000 produced by Nanocyl, Belgium. Table 1 shows the main characteristics of MWCNTs according to the manufacturer. Ultrapure water from a Milli-Q IQ 7000 equipment was used to prepare the MWCNTs dispersions (18.2 MΩ), and 2.5 mm copper desoldering wire were used as electrodes.

2.2. CNTs dispersions

MWCNTs were dispersed in 25 mL of solution (water/dispersing agent in a 10 mM concentration) in three steps: (i) the dispersant agent was firstly mixed with ultrapure water; (ii) the solution without CNTs was put on a magnetic stirrer for 5 min at 350 rpm; (iii), MWCNTs in the solid concentration of 0.35% by mass of cement were added and then sonicated. Three dispersing agents (TX-100, SikaPlast-328, and EUCON 37) were tested as dispersing agents using an ultrasonic tip set to 40% of amplitude at room temperature. The ultrasonic tip worked continuously in 20 s on/20 s off cycles to avoid overheating [44]. The sonication energies per mass of solution were set to 190 J/g, 390 J/g, and 590 J/g. Therefore, each increase of energy per mass took a different sonication time.

Table 2
Cement paste samples prepared for the experiments, grouped as three reference cement samples without fillers, and three groups of cement samples doped with MWCNTs dispersed in EUCON 37 (Group 1), TX-100 (Group 2), and Sika-Plast-328 (Group 3).

	Reference	Group 1	Group 2	Group 3
Quantity	3	3	3	3
Labels	G0a, G0b, G0c	G1a, G1b, G1c	G2a, G2b, G2c	G3a, G3b, G3c
Composition	Cement 60 g/water 28 mL	Cement 60 g/(water/EUCON 37/MWCNTs) 28 mL	Cement 60 g/(water/TX-100/MWCNTs) 28 mL	Cement 60 g/(water/SikaPlast-328/MWCNTs) 28 mL
Sonication	0 J/g	190 J/g	390 J/g	590 J/g

2.3. MWCNT/cement composites

Cement pastes were prepared with a water/cement ratio of 0.47. At this stage, the aqueous solution is a dispersion of water/dispersing agent/MWCNTs sonicated at a specific energy, as shown in Table 2. Cement paste was hand-mixed and poured in 60 mm height and 30 mm diameter cylindrical molds, maintaining the diameter to height proportion recommended by the standard ASTM C349-18 [45]. The molds had two holes in the axial direction separated 20 mm from each other and centered at the cylinder height. In both holes, desoldering copper wire was inserted as measuring electrodes. Once the molds were filled with cement paste, they were placed on a vibrating table for 10 min and remained in the molds for 48 h. Next, the solid cement samples were cured, submerged in ultrapure water for 28 days, and dried in an oven at 40 °C for 24 h [27]. The purpose of the curing and drying stages was to minimize the effect of ionic conduction on cement-based composites, which can be considered high when the cement contains a substantial amount of free water, as suggested by Wen and Chung [46]. Three cement samples for each dispersing agent were prepared, as well as three reference samples, as shown in Table 2.

2.4. Characterization

After sonication, the dispersions were diluted in ultrapure water in a proportion of 1:100 (ultrapure water 10 mL of dispersion 0.1 mL). The resulting diluted samples were covered in dark vessels to avoid any photoreaction. Light absorbance Ultraviolet–Visible (UV–Vis) and Dynamical Light Scattering (DLS) experiments were performed. The cement-based MWCNTs samples were analyzed by SEM after cutting the samples into 10 mm cubes. Furthermore, electrical impedance spectroscopy (EIS) measurements were conducted on the solid samples. The aforementioned measurements are described in Table 3. Moreover, the MWCNTs particle size distribution was measured by DLS, and each sample was tested in triplicate. The resulting particle sizes were obtained as an average from six measurements. Concerning electric measurements, EIS was measured through the copper electrodes embedded into the cement samples (see Fig. 1). The potentiostat/galvanostat applied a harmonic voltage of amplitude 10 mV (potentiostat mode) to 71 frequency values between 0.1 Hz–1 MHz; the device averages ten measures for each frequency point. The measured data are the amplitude and phase response of the electrical currents, which gives the electrical impedance represented as Nyquist or Bode plots.

2.5. Experimental data processing

The EIS experimental data were analyzed by Python scripts used to perform: (i) geometrical analysis of the Nyquist plots (semicircles and diffusion process); (ii) fitting circuital models and determination of their passive elements; (iii) fitting of the GEMTIP model and extraction of its physical parameters; (iv) data processing, drawing Nyquist, and Bode plots, UV–Vis spectra, and computation of the relative frequency of particle sizes. The python scripts were incorporated in a module that instances each library, exports figures, and organizes the data on data frames. A basin-hopping optimization algorithm was selected to fitting the experimental data taking as residuals the mean squared errors between the predictions of the GEMTIP model and the experimental data [47,48]. Furthermore, an HTML5 with javascript hypertext was created to visualize and analyze the figures. On the other hand, the parameters of the equivalent lumped circuits were extracted fitting the EIS experimental data from software ZView 4.0b.

3. Results and discussion

3.1. Dispersions analysis

MWCNTs dispersions after different sonication energies presented a π-plasmon between 250 nm and 300 nm as shown in Fig. 2, which is within the characteristic range of well-dispersed MWCNTs [49]. Conversely, the samples dispersed with EUCON 37 and TX-100 exhibit additional absorption bands under 250 nm, which are characteristic of the aromatic compounds present in the molecular structure of the dispersing agents [49,50]. The dispersing agent affects the π-plasmon by the amount of energy applied during the dispersion process; SikaPlast-328 π-plasmon was observed at 258 ± 3 nm, EUCON 37 at 288 ± 1 nm, and TX-100 at 275 ± 1 nm (see Fig. 2) which are within the range commonly found for well-dispersed MWCNTs [51,52]. The observed highest plasmon absorbance peak at 1.26 ± 0.15 AU suggests a separation between MWCNTs dispersed with TX-1000 in comparison with other dispersing agents [53]. This higher dispersing efficiency can be associated with the aromatic compounds from polymeric chains interacting with MWCNTs and increasing the affinity between the dispersant agent and MWCNTs [54,55]. A bimodal particle size distribution was found in MWCNTs dispersed with SikaPlast-328, EUCON 37, and TX-100 as shown Fig. 3; the first peak (left-hand side dots in Fig. 3) has a maximum between 30 and 98 nm, while the second peak (right-hand side dots in Fig. 3) is found between 636 and 5600 nm.

3.2. Pore size estimation by SEM images

An analysis of pore sizes was performed by SEM images of cement pieces of 1 cm^2 made of MWCNTs dispersed in EUCON 37, SikaPlast-328, and TX-100. SEM images with 100× of amplification were used to identify the location and images of the pores with 400× of amplification to estimate the pore size, Fig. 4. Pore distribution and average pore size were explored in an area of 5% for each group of MWCNTs/cement composites (see groups description in Table 2), where 50 pores, in average, were measured by SEM image. An average diameter of 159 μm was observed in samples of group 2; 16 μm, in group 1, and 46 μm, in group 3. The observed differences in the pore sizes may be due to air trapped during the paste mixing of the paste, increasing the number and size of pores Such an effect has been previously observed in TX-100 surfactant (group 2) in Ref. [26]; these observations suggest that in the fabrication of group 2 samples, many bubbles were entrapped into cement paste. Such bubbles remained even after putting the samples on a controlled vibration table.

Table 3
Equipment used to characterize the dispersions and cement-based nanomaterials.

Equipment	Supplies	Description	Manufacturer
UV–Vis Spectrometer 8453	10 mm optical path quartz cuvettes	The spectrometer uses deuterium discharge and tungsten lamps for a wavelength range of 190–1100 nm	Agilent
Particle Analyzer Litesizer 500	Quartz cuvettes 10 × 10 × 45 mm, thermal insulation cover	Particle size distribution was measured by DLS at a 90° angle	Anton Paar
Scanning Electron Microscope (SEM)	Images were obtained with an Everhart Thornley ETD for secondary electrons	FEI QUANTA FEG 650 SEM was used with an acceleration voltage of 25 kV	FEI Company
Potentiostat/Galvanostat PGSTAT204	Standard cell cable, dummy cell	PGSTAT204 uses a module FRA32M. Its potential range is −10 V to 10 V, the current range is 10 nA to 100 mA, and the input impedance is 100 GΩ	Metrohm Autolab

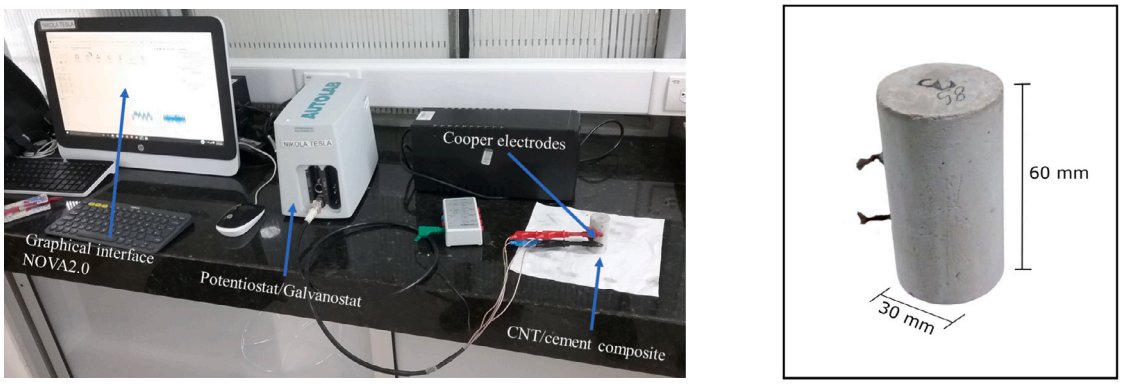

Fig. 1. (a) Experimental setup to perform EIS measurements on CNT/cement composites, and (b) detail of one of the experimental samples (G0a).

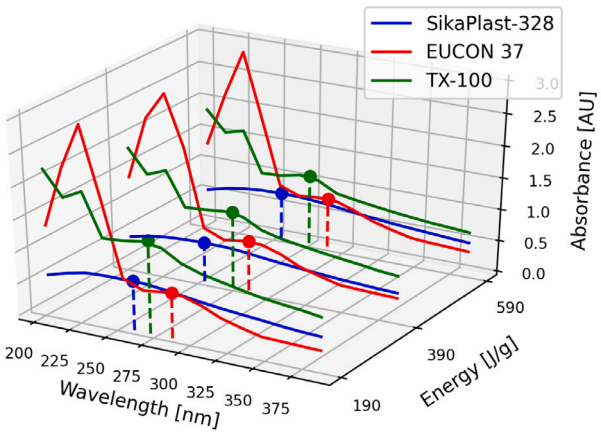

Fig. 2. UV–Vis spectra of MWCNTs dispersed with three surfactants and varying sonication energies: 190 J/g, 390 J/g, and 590 J/g. The points correspond with the CNTs π-plasmon for each curve.

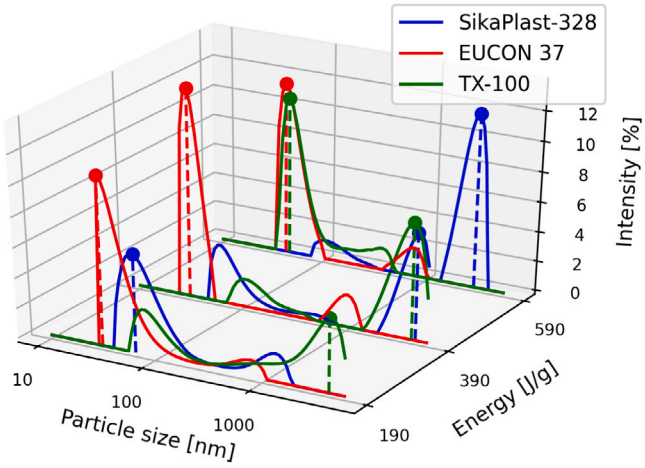

Fig. 3. Particle size distributions of MWCNTs dispersed in SikaPlast-328, EUCON 37, TX-100 at 190 J/g, 390 J/g, and 590 J/g. The points correspond with the highest intensity and their respective mean particle size value for each curve.

3.3. Circuital model and Nyquist plots

The electrical circuit model proposed by Li et al. [29,56] for modeling MWCNTs in cement paste assumed no changes in the charge diffusion process and used a Warburg element to reproduce the behavior of CNTs interacting with the electrodes. However, a charge diffusion process has been observed at very low frequencies in electrical impedance spectra of cement paste with MWCNTs, suggesting an interaction between cement-electrodes [17] and MWCNTs-cement-electrodes [56]. To incorporate these observations, we propose a variant of Li et al. and Zhang et al. [34] model, where we change the Warburg element by a constant phase element CPE, Fig. 5. As a result, the impedance of the proposed equivalent circuit model Z is given by,

$$Z = R_s + \frac{R_{ct1} + Z_W}{1 + j\omega C_1(R_{ct1} + Z_W)} + \frac{R_{ct2} + Z_{CPE}}{1 + j\omega C_2(R_{ct2} + Z_{CPE})}, \quad (1)$$

where R_s is the bulk resistance; C_1 and C_2 are the double layer capacitance between cooper electrodes/cement and MWCNTs/cement, respectively; R_{ct1} and R_{ct2} are the electrical charge transfer resistance

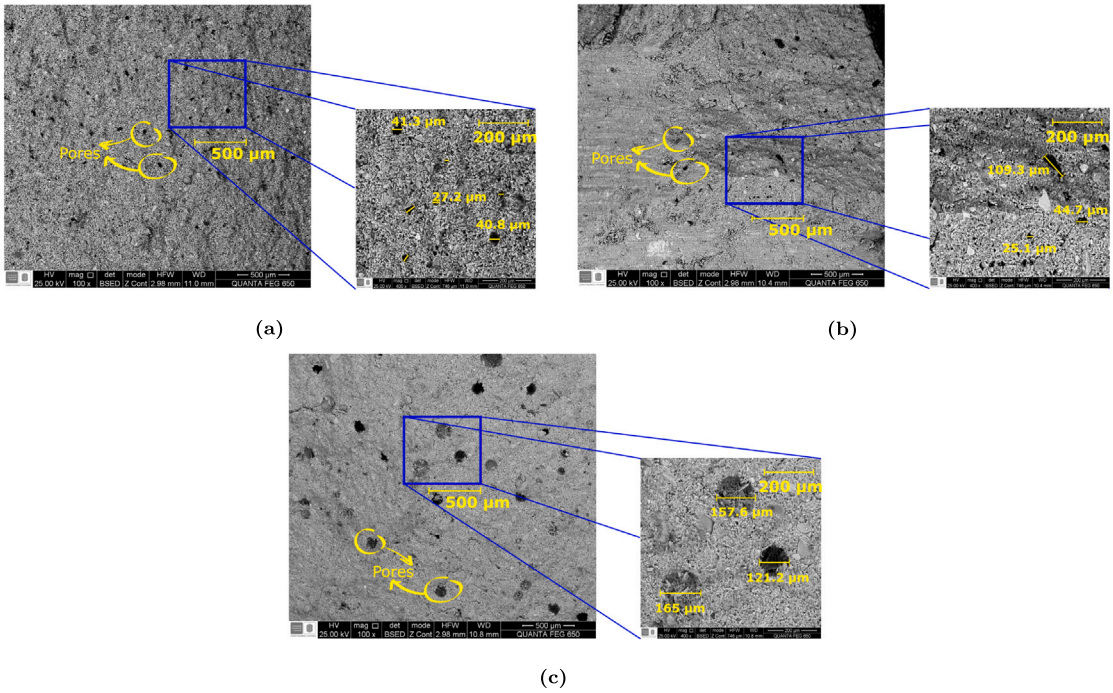

Fig. 4. SEM of cement paste mixed with MWCNTs dispersed in (a) EUCON 37, (b) SikaPlast-328, and (c) TX-100.

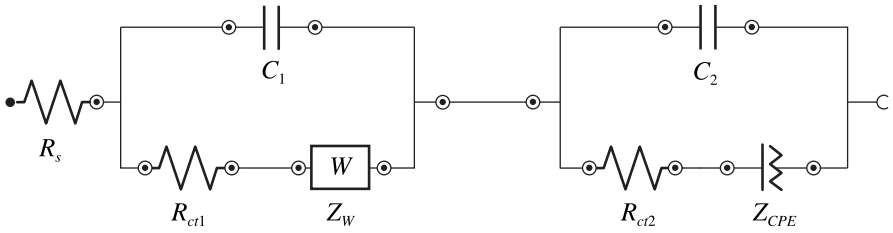

Fig. 5. Electrical circuit model of MWCNTs/cement composites.

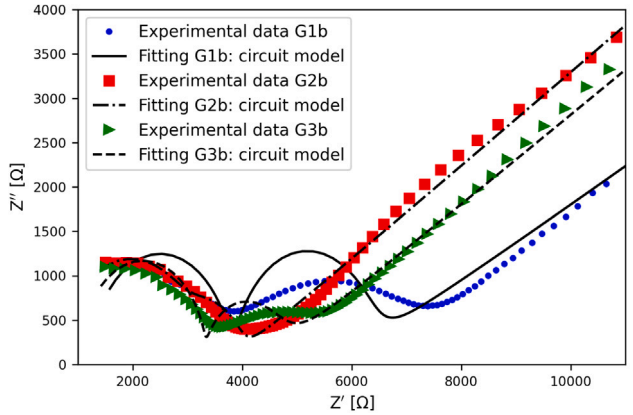

Fig. 6. Nyquist plots of the samples G1b, G2b, and G3b compared with the predicted results from the equivalent lumped circuit.

of copper electrodes and MWCNTs, respectively; Z_W and Z_{CPE} are the constant phase element and Warburg element that explain the diffusion of ions in electrodes-cement and MWCNTs-cement interphase, respectively. On the other hand, The Warburg element Z_W relates to the electrical conductivity of the cement paste, $Z_W = \sigma\omega^{-1/2}(1-j)$ [29], with σ being the conductivity of CNTs, ω the angular frequency, and the imaginary number $j = \sqrt{-1}$. The impedance of the constant phase element Z_{CPE} can be expressed as $Z_{CPE} = T^{-1}(j\omega)^{-n}$, where T is a pseudocapacitance, and n is a parameter between 0 to 1. This element defines the resistive or capacitive behavior of the constant phase element. In Appendix A we show the Li et al. [29,56] model is recovered as a particular case of the proposed model.

According to the proposed equivalent circuit model, the experimental Nyquist plots for the samples G1b, G2b, and G3b were used to fit the circuit model. The obtained model parameters are reported in Table 4.

The slope of the diffusion process changes for different dispersant agents can be observed in Fig. 6. This fact may be ascribed to the diffusion of electrode ions to the cement-based material. The delay in the diffusion effect achieves the minimum increment in the slope at low frequencies when using the TX-100 dispersant compared to EUCON 37 or SikaPlast-328. It is also noted in Fig. 6 that the circuital model for samples G1b and G3c does not perform well. Chi-square values of $1.34E-2$ and $6.70E-2$ were found for G1b and G3c, respectively, while the chi-square value for G2b was $1.42E-3$, G1b and G3b. Then, the best data fit was found for cement samples prepared with TX-100 because its Nyquist diagram does not show a second semicircle that would be present if MWCNTs were well dispersed. Interestingly, the results by Dong et al. [29] reported good agreements between experiments and the estimates by the model presented in Eq. (1), considering a Warburg impedance instead of the CPE. Those results correspond to a special case where the slope of the diffusion process is equal to one. In contrast, the results presented herein evidence that equivalent circuit models considering only Warburg elements cannot accurately describe the diffusion process of MWCNTs/cement composites.

Table 4
Parameters of the circuital model proposed for MWCNTs/cement composites.

Sample	R_s [Ω]	R_{cr1} [Ω]	R_{cr2} [Ω]	C_1 [F]	C_2 [F]	σ [Ω m]	T [Fs^{n-1}]	n
G1b	1240	2141	2361	5.2×10^{-8}	1.6×10^{-10}	78.6	2.0×10^{-4}	0.25
G2b	748	809	2129	3.5×10^{-9}	1.1×10^{-10}	330.4	8.9×10^{-5}	0.30
G3b	1017	2319	1043	1.5×10^{-10}	3.3×10^{-8}	117.9	1.6×10^{-4}	0.29

3.4. GEMTIP model with cylindrical inclusions and spherical macropores

Zhdanov [38] developed a new theory to describe the propagation of low-frequency electromagnetic waves on heterogeneous medium considering the effective medium approach but including the induced polarization phenomena. Whith his theory, Zhdanov obtains a tensorial expression to the effective conductivity of heterogeneous media, Eq. (B.1). As a particular study case, Zhdanov obtained the explicit expression of effective conductivity σ_e for ellipsoidal and spherical shapes; here, we derivate an expression to cylindrical inclusions, where the volume, $\hat{\Gamma}$, and surface, $\hat{\Lambda}$, depolarization tensors taken a different form than for spherical inclusions, as we show in details in Appendix B.

The electrical conductivity contribution of cylindrical inclusions, σ_{cyl}, in terms of the volume, $\hat{\Gamma}$, and surface, $\hat{\Lambda}$, depolarization tensors derived in Appendix B is expressed in terms of polarizability $M_1 = 2\frac{(\rho_0-\rho_1)}{(\rho_0+\rho_1)}$ and relaxation time $\tau_1 = \left[a_1\alpha_1^{-1}\left(\rho_0+\rho_1\right)\right]^{1/C_1}$ as follows:

$$\sigma_{cyl} = \frac{1}{\rho_0} f_1 M_1 \left[1 - \frac{1}{1+\left(j\omega\tau_1\right)^{C_1}}\right], \tag{2}$$

with f_1 being the volume fraction of MWCNTs, ρ_0 is the electrical resistivity of the background, while ρ_1 is the resistivity of MWCNTs. Finally, α_1, C_1, τ_1 are the surface-polarizability coefficient, coefficient of MWCNTs, and the relaxation time, respectively.

In this work we model the macropores into the cement samples as spherical inclusions, then, the contributions to electrical conductivity of macropores corresponds with the expression obtained by Zhdanov [38] in terms of polarizability $M_l = 3\frac{(\rho_0-\rho_l)}{(\rho_0+\rho_l)}$, and relaxation time $\tau_l = \left[\frac{1}{2}a_l\alpha_l^{-1}\left(\rho_0+2\rho_l\right)\right]^{1/C_l}$; its contribution to the electrical conductivity of effective medium is $\Delta\sigma_b$. In this sense and as a consequence of Eq. (B.20), the electrical conductivity σ_e of effective medium is given by,

$$\sigma_e = \frac{1}{\rho_0} + \sigma_{cyl} + \Delta\sigma_b. \tag{3}$$

In terms of the electrical resistivity $\rho_e = 1/\sigma_e$ of the effective medium,

$$\frac{1}{\rho_e} = \frac{1}{\rho_0} + \sigma_{cyl} + \frac{1}{\rho_0}\sum_{l=2}^{N} f_l M_l \left[1 - \frac{1}{1+\left(j\omega\tau_l\right)^{C_l}}\right]. \tag{4}$$

To build the effective electrical impedance Z_e from effective resistivity ρ_e, we considered the cylindrical shape of samples, where the electrical current flows through its cross-sectional area. Therefore, the resistivity was multiplied by a geometrical factor given by the length between electrodes (L = 20 mm) divided by the circular transverse surface area A (radius of 15 mm) of the cylindrical cement samples,

$$Z_e = \frac{L}{A}\rho_e. \tag{5}$$

3.5. Data interpretation using the GEMTIP model

The proposed model is in the framework of classical electromagnetic theory. Therefore, the model presented in Eq. (5) does not have quantum components, whose role may be critical for volume fractions below the percolation threshold [57]. Nonetheless, this is not a limitation of this model, which is used to describe the electric properties of CNTs over the percolation threshold, as is shown in the following model proposed by Kumar and Rawal [58],

$$f_c = \frac{\pi}{5.77sI}, \tag{6}$$

with s being the aspect ratio of the fillers, and I, an orientation parameter defining the orientation characteristics of nanofillers in the assembly; as there is no deformation on the samples $I = 1.27327$ [15], and the aspect ratio $s = 181$. In this work, term s was determined from carbon nanotube dimensions obtained through SEM images of the same batch by Mendoza-Reales [59], and particle size (see Section 3.2). According to Eq. (6), it has been estimated that all the cement samples fabricated in this research (with a MWCNTs volume fraction of $f_1 = 0.35\%$), contains MWCNTs after percolation threshold of $f_c = 0.23\%$, thereby the applicability of the proposed formulation is guaranteed.

Although this work does not explicitly include quantum-mechanical mechanisms, percolated (agglomerated) and non-percolated (non-agglomerated) MWCNTs effects can still be differentiated when making a frequency sweep on the cement samples; this is because the cement-based composites contain heterogeneous agglomerated and non-agglomerated nanotubes during their manufacture. In addition, depending on the dispersant agent, a higher proportion of agglomerated and non-agglomerated CNTs were found, as shown in Fig. 7. We did obtain the molar fraction of pores f_p, the surface-polarizability coefficient of pores, α_p, and MWCNTs, α_1, Table 5, by inverse modeling through the optimization of the mean square error between experimental data and Eqs. (4) and (5), using a basin-hopping optimization algorithm. The volume fraction occupied by macropores and size pore families shown in Table 6 are into ranges reported by Cabeza et al. [28]. Therefore, it is concluded that the proposed approach allows one to characterize the volume pore fraction from electrical impedance measurements without mercury intrusion porosimetry measurements.

The surface-polarizability coefficients α let us know how the polarization induction from electric charges on the surface of inclusions, i.e., pores and MWCNTs, may induce at the same time effective electrical currents between separated inclusions that contribute to diminishing the distance from the low and high-frequency real part of impedance, i.e., $real\{Z\}_{\omega\to 0} - real\{Z\}_{\omega\to\infty}$. From experimental data,

Table 5
Some GEMTIP parameters from electrical impedance spectra of cement-based MWCNTs.

Sample	α_1 [Ω m^2/s^{C_1}]	α_p [Ω m^2/s^{C_p}]	f_p [%]
G1a	4.0×10^{-4}	1.9×10^{16}	30.9
G1b	3.5×10^{-3}	5.8×10^{11}	20.1
G1c	2.2×10^{-3}	1.7×10^{12}	16.0
G2a	6.0×10^{-6}	1.6×10^{12}	31.0
G2b	6.0×10^{-6}	1.6×10^{12}	32.0
G2c	7.0×10^{-6}	1.6×10^{12}	27.7
G3a	1.2×10^{-4}	3.7×10^{11}	9.9
G3b	1.0×10^{-2}	3.7×10^{11}	33.3
G3c	9.7×10^{-5}	3.6×10^{13}	25.0

Table 6
Pore volume fractions according to the average size of pores into the cement samples.

Samples	f_p [%]	Family pore size [μm]
G1a, G1b, G1c	22	30
G2a, G2b, G2c	30	159
G3a, G3b, G3c	23	36

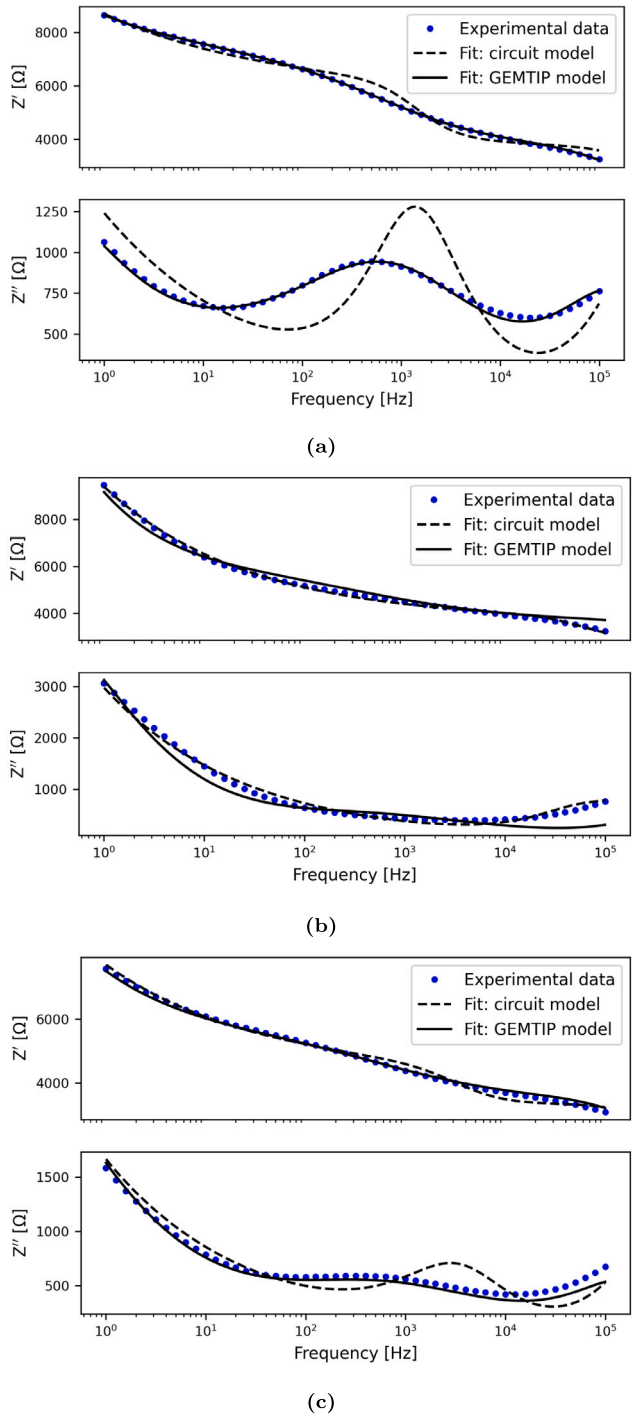

Fig. 7. Bode plots of cement samples doped with MWCNTs dispersed with (a) EUCON 37 (G1b), (b) TX-100 (G2b), and (c) SikaPlast-328 (G3b) in comparison with the models GEMTIP and lumped equivalent circuit.

we obtained low values of the surface-polarizability coefficients of MWCNTs α_1, as shown in Table 5. Furthermore, the large values of the surface-polarizability coefficients in the pores α_p show the difficulty of inducing an electrical charge polarization on their surface; in this way, the surface-polarizability coefficient of cement samples that contain TX-100 (for example, G2b) increases until 1.9×10^{16} $\Omega m^2/s^{C_1}$.

Fig. 7 shows the Bode plots of cement samples containing EUCON 37, TX-100, and SikaPlast-328. In detail, Fig. 7(a) presents a peak on the imaginary part of the impedance, which is related to the capacitive properties of the samples. These properties are certainly due to the excellent quality of the dispersions of the samples containing EUCON 37 as observed during the UV–Vis and particle size analyses in Sections 3.2 and 3.3 Therefore, in the considered frequency range (10 Hz–10 kHz), the relaxation time of the samples indicates that most of the contribution to the electric charge transport is induced by an electric relaxation of MWCNTs. Moreover, the cement samples with SikaPlast-328 exhibit a smaller capacitive contribution compared to samples with EUCON 37, Fig. 7(c). Finally, a purely resistive behavior in the frequency range (10 Hz–10 kHz) is observed in the impedance spectra of the samples with TX-100, Fig. 7(b), indicating that the electrical charge transport is governed by the electrical charge transfer between adjacent MWCNTs (percolated MWCNTs). It is known that pores produce several dispersions at high frequencies in the range 10 kHz–15 MHz [28]. Accordingly, Figs. 7(a) and 7(c) present a local minimum in the imaginary part of the impedance for frequencies over 10 kHz. Therefore, we consider the local minimum as a negative dispersion from pores over the sum in Eq. (B.20c) because the pore's resistivity is larger than the cement matrix $\rho_0 \gg \rho_l$. For this reason, M_l tends to −3. Under these assumptions, the imaginary part of the impedance was in agreement with the GEMTIP model, as it is shown in Fig. 7 in the shape of the valleys appearing around 10^4 Hz.

4. Conclusions

In this work, the electrical response in AC of cement/CNT composites was interpreted by an effective medium model. Furthermore, a lumped circuit model previously reported in the literature has been modified to fit the electrical impedance of three different cement-based composites. The presented GEMTIP model allows a physically robust interpretation of the AC impedance of cement/CNT composites, allowing for analysis of the contribution of the main micromechanical properties of these composites and, thus, offering a vast potential for materials design. The main conclusions of this work can be summarized as follows:

- A better description of the electrical response in AC was achieved using the effective medium model compared to the lumped circuit model, with the advantage of obtaining information on the filler volume fraction directly from the model parameters.
- The lumped circuit model could not describe the electrical impedance of cement samples doped with MWCNTs dispersed with EUCON 37 and SikaPlast-328. Moreover, to describe the electrical impedance of the cement samples with TX-100, an unconventional circuital element to describe the diffusion process (low frequencies) has been included. Therefore, the Warburg element that defines the CNTs interaction with electrodes has been replaced for a constant phase element to fit the Nyquist plots of cement samples with TX-100.
- The real and imaginary parts of the electrical impedance of cement/MWCNTs composites have been modeled by the generalized effective medium approach considering cylindrical inclusions, i.e., by the proposed effective medium model.
- Remarkably, the effective medium model has shown low values on the function to be optimized or good fit quality (around 0.002 Ω/Ω) no matter the shape of the electrical impedance spectra. The volume fraction of MWCNTs, the average size of pores, and the real dimensions of MWCNTs have been taken from experimental characterization results and excluded from the model calibration. In particular, the latter two parameters have been obtained from DLS measurements, SEM images, and the first one from the dispersion preparation methodology.

As a result of the proposed model, the highest pores volume fraction was calculated for cement/MWCNTs samples with TX-100 (≈30%), lower values were obtained for SikaPlast-328 (23%) and EUCON 37 (22%). Concerning the cement samples with TX-100, the macropores enabled a more significant agglomeration of MWCNTs forming conductive paths and, accordingly, they also decreased the surface polarizability factor α_1 until 4×10^{-4} [$\Omega m^2/s^{C_1}$].

CRediT authorship contribution statement

Daniel A. Triana-Camacho: Investigation, Formal analysis, Writing – original draft, Writing – review & editing, Conceptualization, Methodology, Validation, Software. **David A. Miranda:** Writing – review & editing, Formal analysis, Data curation, Software. **Enrique García-Macías:** Writing – review & editing, Resources, Visualization. **Oscar A. Mendoza Reales:** Writing – review & editing, Formal analysis, Data curation. **Jorge H. Quintero-Orozco:** Supervision, Funding acquisition, Resources, Validation, Writing – review & editing.

Declaration of competing interest

The authors declare that they have no known competing financial interests or personal relationships that could have appeared to influence the work reported in this paper.

Data availability

Data will be made available on request.

Acknowledgments

The authors would like to acknowledge the financial support from the *ICETEX* through the funds program 890 of *MinCiencias* by the project number 82779, entitled *Piezoresistividad en Pasta de Cemento con Adición de Nanopartículas de Oro o Materiales Carbonosos*. We want to give special thanks to scholarships program of *MinCiencias Programa de Becas de Excelencia Doctoral del Bicentenario - Corte 2, 2019*. E. García-Macías was supported by the Consejería de Transformación Económica, Conocimiento, Empresas *y* Universidades de la Junta de Andalucía (Spain) through the research project P18-RT-3128. Funding for open access charge: Universidad de Granada/CBUA.

Appendix A. Analysis of circuital model

Using Moivre's formula [60], Z_{CPE} takes the form:

$$Z_{CPE} = T^{-1}\omega^{-n}\left[\cos\left(\frac{\pi}{2}n\right) - j\sin\left(\frac{\pi}{2}n\right)\right] = T^{-1}\omega^{-n}(a - jb). \tag{A.1}$$

On this basis, the effective impedance in Eq. (1) can be rewritten as:

$$Z = \underbrace{R_s}_{Z_I} + \underbrace{\frac{R_{ct1} + \sigma\omega^{-1/2}(1-j)}{1 + j\omega C_1[R_{ct1} + \sigma\omega^{-1/2}(1-j)]}}_{Z_{II}} + \underbrace{\frac{R_{ct2} + T^{-1}\omega^{-n}(a-jb)}{1 + j\omega C_2[R_{ct2} + T^{-1}\omega^{-n}(a-jb)]}}_{Z_{III}}. \tag{A.2}$$

After some manipulations, the second term of the impedance in Eq. (A.2) can be extended as:

$$Z_{II} = \frac{R_{ct1} + \sigma\omega^{-1/2}}{(1+\sigma\omega^{1/2}C_1)^2 + (R_{ct1}\omega C_1 + \sigma\omega^{1/2}C_1)^2} - j\frac{\sigma\omega^{-1/2} + 2\sigma^2 C_1 + R_{ct1}^2\omega C_1 + 2R_{ct1}\sigma\omega^{1/2}C_1}{(1+\sigma\omega^{1/2}C_1)^2 + (R_{ct1}\omega C_1 + \sigma\omega^{1/2}C_1)^2} \tag{A.3}$$

Following the same strategy to simplify the third term in Eq. (A.2), it follows that:

$$Z_{III} = \frac{R_{ct2} + T^{-1}\omega^{-n}a}{(1+T^{-1}\omega^{1-n}C_2 b)^2 + (R_{ct2}\omega^2 C_2^2 + T^{-1}\omega^{1-n}C_2 a)^2} - j\frac{T^{-1}\omega^{-n}b + T^{-2}\omega^{1-2n}C_2 + R_{ct2}^2\omega C_2 + 2R_{ct2}T^{-1}\omega^{1-n}a}{(1+T^{-1}\omega^{1-n}C_2 b)^2 + (R_{ct2}\omega^2 C_2^2 + T^{-1}\omega^{1-n}C_2 a)^2}. \tag{A.4}$$

At low frequencies $\omega \to 0$ (DC), the denominators in Eqs. (A.3) and (A.4) tend to 1 and the effective impedance reduces to:

$$Z = \left(R_s + R_{ct1} + R_{ct2} + \sigma\omega^{-1/2} + T^{-1}\omega^{-n}a\right) - j\left(\sigma\omega^{-1/2} + 2\sigma^2 C_1 + T^{-1}\omega^{-n}b + T^{-2}\omega^{1-2n}C_2\right). \tag{A.5}$$

Comparing the real Z' and imaginary Z'' parts of impedance in Eq. (A.5), one can extract the following relation:

$$Z'' = \frac{b}{a}Z' - \frac{b}{a}\left(R_s + R_{ct1} + R_{ct2}\right) + \sigma\omega^{-1/2}\left(1 - \frac{b}{a}\right) + 2\sigma^2 C_1 + T^{-2}\omega^{1-2n}C_2. \tag{A.6}$$

According to Eqs. (A.6) and (A.1), and the Nyquist's diagrams obtained in the experiments at low frequencies, there exists a relation between the slope b/a and the parameter n, as follow:

$$\frac{b}{a} = \frac{\sin(\frac{\pi}{2}n)}{\cos(\frac{\pi}{2}n)} = \tan\left(\frac{\pi}{2}n\right). \tag{A.7}$$

Then,

$$n = \frac{2}{\pi}\arctan\left(\frac{b}{a}\right). \tag{A.8}$$

There are three possibilities for n Eq. (A.6). In the case of $n < 1/2$, term $T^{-2}\omega^{1-2n}C_2$ tends to 0, and $\sigma\omega^{-1/2}\left(1-\frac{b}{a}\right)$ will be positive; for $n = 1/2$, the circuital model reduces to the model proposed by Li et al. [56]; and for $n > 1/2$, which gives the general model in Eq. (A.8), term $\sigma\omega^{-1/2}\left(1-\frac{b}{a}\right)$ becomes negative. The terms that depend on frequency in Eq. (A.6) affect the linearity of the model at low frequencies.

Appendix B. Derivation of GEMTIP depolarization tensors for cylindrical inclusions and its contribution to the electrical conductivity

The conductivity σ_e of effective medium obtained by Zhadanov [38] is given by Eq. (B.1).

$$\sigma_e = \sigma_0 + \sum_{l=1}^{N}[1 - (1 + p_l)\Delta\sigma_l\Gamma_l]^{-1}\Delta\sigma_l f_l. \tag{B.1}$$

With σ_0 being the bulk conductivity; σ_l, the conductivity of inclusions the same shape and size; $\Delta\sigma_l = \sigma_l - \sigma_0$, the difference between conductivities of the inclusion and the bulk; term N stands for the number of inclusions of the lth type; p_l the surface-polarizability of the lth inclusion, and f_l, the volume fraction of a inclusion of the l type. Here p_l can be obtained in terms of the volume Γ_l and surface Λ_l depolarization tensors for the lth inclusion type, and the relative conductivity ξ_l as

$$p_l = \xi_l\Gamma_l^{-1}\Lambda_l. \tag{B.2}$$

where the relative conductivity depends on the surface-polarizability factor k_l as $\xi_l = k_l\sigma_0\sigma_l\Delta\sigma_l^{-1}$. Substituting Eq. (B.2) into Eq. (B.1), one obtains:

$$\sigma_e = \sigma_0 + \sum_{l=1}^{N}\left[1 - \left(1 + k_l\sigma_0\sigma_l\Delta\sigma_l^{-1}\Gamma_l^{-1}\Lambda_l\right)\Delta\sigma_l\Gamma_l\right]^{-1}\Delta\sigma_l f_l. \tag{B.3}$$

It was considered a cylindrical shape for the first type of inclusions $l = 1$. Next, we must get the volume depolarization tensor $\hat{\mathbf{\Gamma}}_1$ for cylindrical inclusions (sketched in Fig. B.8) as:

$$\hat{\mathbf{\Gamma}}_1 = \iiint_V \hat{\mathbf{G}}_b(\mathbf{r}, \mathbf{r}')\,dv'. \tag{B.4}$$

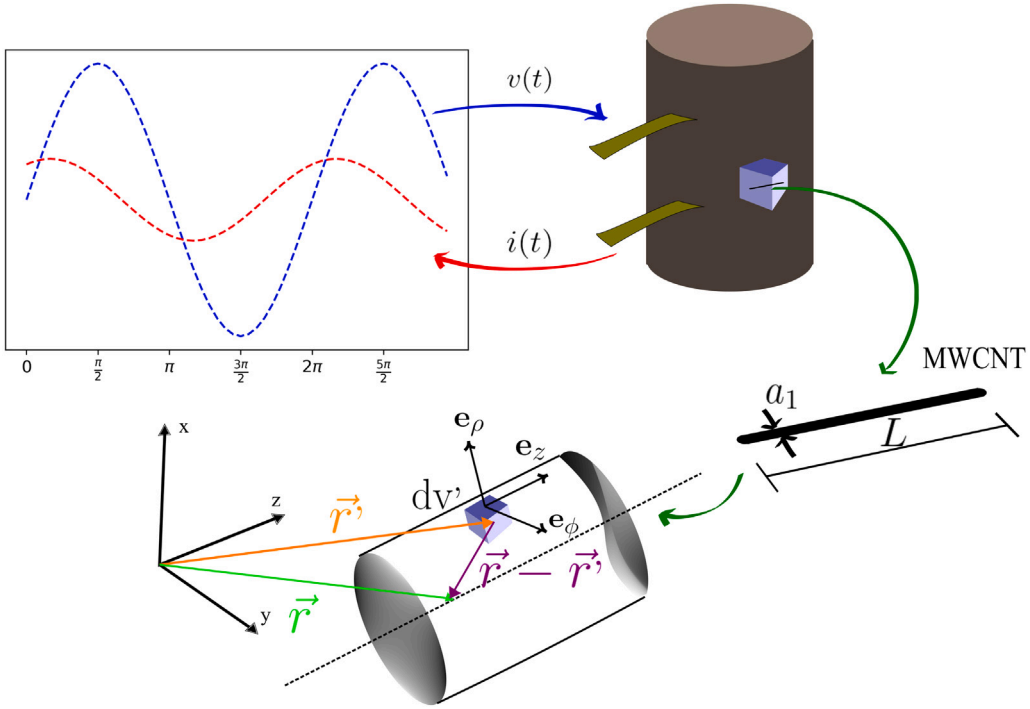

Fig. B.8. The multiscale problem of MWCNTs/cement composite excited by an AC signal.

where $\hat{\mathbf{G}}_b$ is a Green's tensor defined as a dyadic operator acting over a Green's function $g_b(\mathbf{r},\mathbf{r}')$, the vector $\mathbf{r}$ depicts spatial position, ans the vector $\mathbf{r}'$ is the differential volume element $\mathrm{d}v'$. In addition, taking into account that $g_b(\mathbf{r},\mathbf{r}')$ satisfies the Poisson equation $\sigma_b \nabla'^2 g_b = -\delta(\mathbf{r}-\mathbf{r}')$, and the boundary conditions for a surface in infinite such that $g_b|_\infty = 0$ and $\partial g_b/\partial n'|_\infty = 0$, it obtains the Green's function of free space $g_b(\mathbf{r}, is derived as \mathbf{r}') = \frac{1}{4\pi\sigma_0|\mathbf{r}-\mathbf{r}'|}$. Hence, Green's tensor is written as:

$$\hat{\mathbf{G}}_b = \nabla\nabla' g_b(\mathbf{r},\mathbf{r}'). \tag{B.5}$$

Combining Eqs. (B.4) and (B.5), and using the Gauss' theorem, one gets.

$$\hat{\mathbf{\Gamma}}_1 = \iint_S \nabla g_b(\mathbf{r},\mathbf{r}')\,\mathbf{n}(\mathbf{r}')\,\mathrm{d}s'. \tag{B.6}$$

where $\mathbf{n}(\mathbf{r}')$ is a unit vector normal to the cylindrical shape. Solving ∇g_b result.

$$\nabla g_b(\mathbf{r},\mathbf{r}') = \frac{\mathbf{r}-\mathbf{r}'}{4\pi\sigma_0|\mathbf{r}-\mathbf{r}'|^3}. \tag{B.7}$$

Combining Eqs. (B.6) and (B.7), we have the following relation.

$$\hat{\mathbf{\Gamma}}_1 = \frac{1}{4\pi\sigma_0}\iint_S \frac{\mathbf{r}-\mathbf{r}'}{|\mathbf{r}-\mathbf{r}'|^3}\mathbf{n}(\mathbf{r}')\,\mathrm{d}s'. \tag{B.8}$$

In the center of cylinder $r = 0$, and Eq. (B.8) takes the following form:

$$\hat{\mathbf{\Gamma}}_1 = -\frac{1}{4\pi\sigma_0}\iint_S \frac{\mathbf{r}'}{|\mathbf{r}'|^3}\mathbf{n}(\mathbf{r}')\,\mathrm{d}s', \tag{B.9}$$

the differential area in cylindrical coordinates reads.

$$\mathrm{d}s' = a_1\mathrm{d}\varphi\mathrm{d}z, \tag{B.10}$$

where a_1 is the CNT's radius. Then, using $r'^2 = a_1^2 + z^2$; $\mathbf{r}' = a_1\mathbf{e}_\rho + z\mathbf{e}_z$; $\mathbf{n} = \mathbf{e}_\rho$; and replacing Eq. (B.10) into (B.9), we obtain:

$$\hat{\mathbf{\Gamma}}_1 = -\frac{1}{4\pi\sigma_0}\int_{z=-\frac{L}{2}}^{z=\frac{L}{2}}\int_{\varphi=0}^{\varphi=2\pi}\frac{a_1\mathbf{e}_\rho + z\mathbf{e}_z}{\left(a_1^2+z^2\right)^{\frac{3}{2}}}\mathbf{e}_\rho a_1\mathrm{d}\varphi\mathrm{d}z. \tag{B.11}$$

Being $\mathbf{e}_\rho = \mathbf{e}_x\cos(\varphi) + \mathbf{e}_y\sin(\varphi)$, and separating the integral one gets.

$$\hat{\mathbf{\Gamma}}_1 = \frac{\hat{\mathbf{\Gamma}}_{1a} + \hat{\mathbf{\Gamma}}_{1b}}{4\pi\sigma_0}, \tag{B.12a}$$

$$\hat{\mathbf{\Gamma}}_{1a} = -\int_{z=-\frac{L}{2}}^{z=\frac{L}{2}}\int_{\varphi=0}^{\varphi=2\pi}\frac{a_1^2\mathbf{e}_\rho\mathbf{e}_\rho}{\left(a_1^2+z^2\right)^{\frac{3}{2}}}\mathrm{d}\varphi\mathrm{d}z, \tag{B.12b}$$

$$\hat{\mathbf{\Gamma}}_{1b} = -\int_{z=-\frac{L}{2}}^{z=\frac{L}{2}}\int_{\varphi=0}^{\varphi=2\pi}\frac{a_1 z\mathbf{e}_z\left[\mathbf{e}_x\cos(\varphi) + \mathbf{e}_y\sin(\varphi)\right]}{\left(a_1^2+z^2\right)^{\frac{3}{2}}}\mathrm{d}\varphi\mathrm{d}z. \tag{B.12c}$$

where the dyadic product of unitary vectors has been considered, that is $\mathbf{e}_\rho\mathbf{e}_\rho$, $\mathbf{e}_z\mathbf{e}_x$, and $\mathbf{e}_z\mathbf{e}_y$. Furthermore, Eq. (B.12c) is null for the angular integrals over φ. Hence, Eq. (B.12) can be further reduced as:

$$\hat{\mathbf{\Gamma}}_1 = -\frac{a_1^2\pi}{4\pi\sigma_0}\frac{2L}{a_1^2\left(L^2+4a_1^2\right)^{\frac{1}{2}}}\hat{\mathbf{I}}, \tag{B.13}$$

where $\hat{\mathbf{I}}$ is the identity tensor. MWCNTs have a mean diameter a_1 of 19.25 nm [59], while their length L is up to 3.5 μm. Therefore, if CNTs are assumed as infinitely large fillers, i.e. $L \gg a_1$, the depolarization volume gives:

$$\hat{\mathbf{\Gamma}}_1 = -\frac{1}{2\sigma_0}\hat{\mathbf{I}}. \tag{B.14}$$

Next, we got the surface depolarization tensor $\hat{\mathbf{\Lambda}}_1$ from the next formula:

$$\hat{\mathbf{\Lambda}}_1 = \frac{1}{4\pi\sigma_0}\iint_S \nabla\nabla' g_b\cdot\mathbf{n}(\mathbf{r}')\,\mathbf{n}(\mathbf{r}')\,\mathrm{d}s'. \tag{B.15}$$

Solving the gradient of the Green's function ∇g_b, Eq. (B.15) reduces to:

$$\hat{\mathbf{\Lambda}}_1 = \frac{1}{4\pi\sigma_0}\iint_S \nabla'\left[\frac{\mathbf{r}-\mathbf{r}'}{|\mathbf{r}-\mathbf{r}'|^3}\right]\cdot\mathbf{n}(\mathbf{r}')\,\mathbf{n}(\mathbf{r}')\,\mathrm{d}s'. \tag{B.16}$$

If $r = 0$ and $\mathbf{n} = \mathbf{e}_\rho$, the normal derivative reads:

$$\frac{\partial}{\partial a_1}\left(\frac{\mathbf{r}'}{|\mathbf{r}'|^3}\right) = \left(\frac{1}{|\mathbf{r}'|^3}\right)\frac{\partial\mathbf{r}'}{\partial a_1} + \mathbf{r}'\frac{\partial}{\partial a_1}\left(\frac{1}{|\mathbf{r}'|^3}\right). \tag{B.17}$$

Solving $\frac{\partial \mathbf{r}'}{\partial a_1}$, $\frac{\partial}{\partial a_1}\left(\frac{1}{|\mathbf{r}'|^3}\right)$, and replacing them in Eq. (B.16), one can write:

$$\hat{\mathbf{\Lambda}}_1 = \frac{1}{4\pi\sigma_0}\iint_S \left(\hat{\mathbf{\Lambda}}_{1,1} - \hat{\mathbf{\Lambda}}_{1,2}\right)\mathbf{e}_\rho a_1 \mathbf{d}\varphi\mathbf{d}z, \tag{B.18a}$$

$$\hat{\mathbf{\Lambda}}_{1,1} = \frac{\mathbf{e}_\rho}{\left(a_1^2 + z^2\right)^{3/2}}, \tag{B.18b}$$

$$\hat{\mathbf{\Lambda}}_{1,2} = \frac{3a_1\left(a_1\mathbf{e}_\rho + z\mathbf{e}_z\right)}{\left(a_1^2 + z^2\right)^{5/2}}. \tag{B.18c}$$

Considering the orthonormality properties of the unitary vectors e_z and $\mathbf{e}_\rho$, i.e. $\mathbf{e}_\rho\mathbf{e}_\rho = 1$ and $\mathbf{e}_z\mathbf{e}_\rho = 0$, the surface depolarization tensor can be cast into a more compact expression as:

$$\hat{\mathbf{\Lambda}}_1 = -\frac{1}{2\sigma_0 a_1}\hat{\mathbf{I}}. \tag{B.19}$$

Then, replacing Eqs. (B.14) and (B.19) by escalar equations and substituting them in the effective conductivity, see Eq. (B.1), the latter takes the form:

$$\sigma_e = \sigma_0 + \Delta\sigma_a + \Delta\sigma_b, \tag{B.20a}$$

$$\Delta\sigma_a = \left[1 + \left(1 + k_1\sigma_0\sigma_1\Delta\sigma_1^{-1}a_1^{-1}\right)\frac{\Delta\sigma_1}{2\sigma_0}\right]^{-1}\Delta\sigma_1 f_1, \tag{B.20b}$$

$$\Delta\sigma_b = \sum_{l=2}^{N}\left[1 - \left(1 + k_l\sigma_0\sigma_l\Delta\sigma_l^{-1}\Gamma_l^{-1}\Lambda_l\right)\Delta\sigma_l\Gamma_l\right]^{-1}\Delta\sigma_l f_l. \tag{B.20c}$$

Eqs. (B.20b) and (B.20c) are the conductivity contribution of MWCNTs and pores, respectively. Term k_1 is the surface-polarizability factor of MWCNTs. Then, solving Eq. (B.20b) and writing it in terms of the resistivity: $\sigma_0 = 1/\rho_0$, $\sigma_1 = 1/\rho_1$, and $\Delta\sigma_1 = \sigma_1 - \sigma_0$, we get:

$$\sigma_{cyl} = 2f_1\left[\frac{\left(\frac{1}{\rho_1} - \frac{1}{\rho_0}\right)}{\frac{1}{\rho_0} + \frac{1}{\rho_1} + k_1\frac{1}{\rho_0\rho_1}a_1^{-1}}\right], \tag{B.21}$$

calling σ_{cyl} the effective conductivity of the cylindrical inclusions (MWCNTs). Taking an experimental model proposed by Zhdanov [38], as $k_1 = \alpha_1(j\omega)^{-C_1}$, with α_1 being the surface-polarizability coefficient, and C_1 a coefficient of MWCNTs, Eq. (B.21) can be rewritten as follows:

$$\sigma_{cyl} = \frac{2f_1}{\rho_0}\left[\frac{(\rho_0 - \rho_1)}{\rho_1 + \rho_0 + \alpha_1(j\omega)^{-C_1}a_1^{-1}}\right]. \tag{B.22}$$

We replace $x^{-1} = \alpha_1(j\omega)^{-C_1}a_1^{-1}$ into Eq. (B.22) to obtain:

$$\sigma_{cyl} = \frac{2f_1}{\rho_0}\frac{(\rho_0 - \rho_1)}{(\rho_0 + \rho_1)}\left[1 - \frac{1}{1 + (\rho_0 + \rho_1)x}\right]. \tag{B.23}$$

Returning to variable x, Eq. (B.23) transforms in:

$$\sigma_{cyl} = \frac{2f_1}{\rho_0}\frac{(\rho_0 - \rho_1)}{(\rho_0 + \rho_1)}\left[1 - \frac{1}{1 + \left(j\omega\tau_1\right)^{C_1}}\right], \tag{B.24}$$

where $\tau_1 = \left[a_1\alpha_1^{-1}(\rho_0 + \rho_1)\right]^{1/C_1}$ is the relaxation time of the cylindrical inclusions (MWCNTs).

References

[1] A.F. Sosa Gallardo, J.L. Provis, Electrochemical cell design and impedance spectroscopy of cement hydration, J. Mater. Sci. 56 (2) (2021) 1203–1220, http://dx.doi.org/10.1007/s10853-020-05397-6.

[2] J. Chen, Q. Qiu, Y. Han, D. Lau, Piezoelectric materials for sustainable building structures: Fundamentals and applications, Renew. Sustain. Energy Rev. 101 (2019) 14–25, http://dx.doi.org/10.1016/j.rser.2018.09.038.

[3] S.C. Paul, A.S. Van Rooyen, G.P. van Zijl, L.F. Petrik, Properties of cement-based composites using nanoparticles: A comprehensive review, Constr. Build. Mater. 189 (2018) 1019–1034, http://dx.doi.org/10.1016/j.conbuildmat.2018.09.062.

[4] H.Y. Kordkheili, S. Hiziroglu, M. Farsi, Some of the physical and mechanical properties of cement composites manufactured from carbon nanotubes and bagasse fiber, Mater. Des. 33 (2012) 395–398, http://dx.doi.org/10.1016/j.matdes.2011.04.027.

[5] D. Leonaviius, et al., The effect of multi-walled carbon nanotubes on the rheological properties and hydration process of cement pastes, Constr. Build. Mater. 189 (2018) 947–954, http://dx.doi.org/10.1016/j.conbuildmat.2018.09.082.

[6] R. Zhang, X. Cheng, P. Hou, Z. Ye, Influences of nano-TiO2 on the properties of cement-based materials: Hydration and drying shrinkage, Constr. Build. Mater. 81 (2015) 35–41, http://dx.doi.org/10.1016/j.conbuildmat.2015.02.003.

[7] D.R. Bortz, C. Merino, I. Martin-Gullon, Carbon nanofibers enhance the fracture toughness and fatigue performance of a structural epoxy system, Compos. Sci. Technol. 71 (1) (2011) 31–38, http://dx.doi.org/10.1016/j.compscitech.2010.09.015.

[8] N. Jaitanong, et al., Piezoelectric properties of cement based/PVDF/PZT composites, Mater. Lett. 130 (2014) 146–149, http://dx.doi.org/10.1016/j.matlet.2014.05.040.

[9] P.W. Chen, D.D.L. Chung, Improving the electrical conductivity of composites comprised of short conducting fibers in a nonconducting matrix: The addition of a nonconducting particulate filler, J. Electron. Mater. 24 (1) (1995) 47–51, http://dx.doi.org/10.1007/BF02659726.

[10] F. Azhari, N. Banthia, Cement-based sensors with carbon fibers and carbon nanotubes for piezoresistive sensing, Cem. Concr. Compos. 34 (7) (2012) 866–873, http://dx.doi.org/10.1016/j.cemconcomp.2012.04.007.

[11] S. Wen, D. Chung, Cement-based materials for stress sensing by dielectric measurement, Cem. Concr. Res. 32 (9) (2002) 1429–1433, http://dx.doi.org/10.1016/S0008-8846(02)00789-5.

[12] J. Liu, J. Fu, T. Ni, Y. Yang, Fracture toughness improvement of multi-wall carbon nanotubes/graphene sheets reinforced cement paste, Constr. Build. Mater. 200 (2019) 530–538, http://dx.doi.org/10.1016/j.conbuildmat.2018.12.141.

[13] G. Koo, T. Tallman, Frequency-dependent alternating current piezoresistive switching behavior in self-sensing carbon nanofiber composites, Carbon 173 (2021) 384–394, http://dx.doi.org/10.1016/j.carbon.2020.11.018.

[14] E. García-Macías, A. D'Alessandro, R. Castro-Triguero, D. Pérez-Mira, F. Ubertini, Micromechanics modeling of the electrical conductivity of carbon nanotube cement-matrix composites, Composites B 108 (2017) 451–469, http://dx.doi.org/10.1016/j.compositesb.2016.10.025.

[15] F.C. Buroni, E. García-Macías, Closed-form solutions for the piezoresistivity properties of short-fiber reinforced composites with percolation-type behavior, Carbon 184 (2021) 923–940, http://dx.doi.org/10.1016/j.carbon.2021.08.083.

[16] S. Wansom, N. Kidner, L. Woo, T. Mason, AC-impedance response of multi-walled carbon nanotube/cement composites, Cem. Concr. Compos. 28 (6) (2006) 509–519, http://dx.doi.org/10.1016/j.cemconcomp.2006.01.014.

[17] L. Chi, Z. Wang, S. Lu, D. Zhao, Y. Yao, Development of mathematical models for predicting the compressive strength and hydration process using the EIS impedance of cementitious materials, Constr. Build. Mater. 208 (2019) 659–668, http://dx.doi.org/10.1016/j.conbuildmat.2019.03.056.

[18] Y. Ruan, B. Han, D. Wang, W. Zhang, X. Yu, Electrical properties of carbon nanotubes filled cementitious composites, Mater. Res. Express 5 (10) (2018) 105704, http://dx.doi.org/10.1088/2053-1591/aadaf6.

[19] E. García-Macías, R. Castro-Triguero, A. Sáez, F. Ubertini, 3D mixed micromechanics-FEM modeling of piezoresistive carbon nanotube smart concrete, Comput. Methods Appl. Mech. Engrg. 340 (2018) 396–423, http://dx.doi.org/10.1016/j.cma.2018.05.037.

[20] B. Han, K. Zhang, X. Yu, E. Kwon, J. Ou, Electrical characteristics and pressure-sensitive response measurements of carboxyl MWNT/cement composites, Cem. Concr. Compos. 34 (6) (2012) 794–800, http://dx.doi.org/10.1016/j.cemconcomp.2012.02.012.

[21] O.A. Mendoza Reales, et al., Influence of MWCNT/surfactant dispersions on the rheology of Portland cement pastes, Cem. Concr. Res. 107 (2018) 101–109, http://dx.doi.org/10.1016/j.cemconres.2018.02.020.

[22] O.A. Mendoza Reales, et al., Anionic, cationic, and nonionic surfactants used as dispersing agents for carbon nanotubes and their effect on cement hydration, J. Mater. Eng. 33 (11) (2021) 04021325, http://dx.doi.org/10.1061/(ASCE)MT.1943-5533.0003955.

[23] Y. Bai, et al., Aqueous dispersion of surfactant-modified multiwalled carbon nanotubes and their application as an antibacterial agent, Carbon 49 (11) (2011) 3663–3671, http://dx.doi.org/10.1016/j.carbon.2011.05.002.

[24] S.J. Chen, et al., Carbon nanotube–cement composites: A retrospect, IES J. A: Civ. Struct. Eng. 4 (4) (2011) 254–265, http://dx.doi.org/10.1080/19373260.2011.615474.

[25] B. Rodriguez, et al., Carbonation study in a cement matrix with carbon nanotubes, J. Phys. Conf. Ser. 1247 (1) (2019) 012024, http://dx.doi.org/10.1088/1742-6596/1247/1/012024.

[26] O.A. Mendoza Reales, et al., Reinforcing effect of carbon nanotubes/surfactant dispersions in Portland cement pastes, Adv. Civ. Eng. 2018 (2018) 2057940, http://dx.doi.org/10.1155/2018/2057940.

[27] P. de Almeida Carísio, et al., Dispersion of carbon nanotubes with different types of superplasticizer as a dispersing agent for self-sensing cementitious materials, Appl. Sci. 11 (18) (2021) 8452, http://dx.doi.org/10.3390/app11188452.

[28] M. Cabeza, M. Keddam, X. Nóvoa, I. Sánchez, H. Takenouti, Impedance spectroscopy to characterize the pore structure during the hardening process of Portland cement paste, Electrochim. Acta 51 (8) (2006) 1831–1841, http://dx.doi.org/10.1016/j.electacta.2005.02.125.
[29] B. Dong, et al., Electrochemical impedance interpretation of the carbonation behavior for fly ash–slag–cement materials, Constr. Build. Mater. 93 (2015) 933–942, http://dx.doi.org/10.1016/j.conbuildmat.2015.05.066.
[30] M. Cabeza, P. Merino, A. Miranda, X. Nóvoa, I. Sanchez, Impedance spectroscopy study of hardened Portland cement paste, Cem. Concr. Res. 32 (6) (2002) 881–891, http://dx.doi.org/10.1016/S0008-8846(02)00720-2.
[31] B. Díaz, B. Guitián, X.R. Nóvoa, C. Pérez, Conductivity assessment of multifunctional cement pastes by impedance spectroscopy, Corros. Sci. 185 (2021) 109441, http://dx.doi.org/10.1016/j.corsci.2021.109441.
[32] P.A. Danoglidis, M.S. Konsta-Gdoutos, S.P. Shah, Relationship between the carbon nanotube dispersion state, electrochemical impedance and capacitance and mechanical properties of percolative nanoreinforced OPC mortars, Carbon 145 (2019) 218–228, http://dx.doi.org/10.1016/j.carbon.2018.12.088.
[33] Y. Zhu, H. Zhang, Z. Zhang, Y. Yao, Electrochemical impedance spectroscopy (EIS) of hydration process and drying shrinkage for cement paste with W/C of 0.25 affected by high range water reducer, Constr. Build. Mater. 131 (2017) 536–541, http://dx.doi.org/10.1016/j.conbuildmat.2016.08.099.
[34] J. Zhang, et al., Nondestructive monitoring on hydration behavior of cement pastes via the electrochemical impedance spectroscopy method, Measurement 185 (2021) 109884, http://dx.doi.org/10.1016/j.measurement.2021.109884.
[35] J.D. Eshelby, The determination of the elastic field of an ellipsoidal inclusion, and related problems, Proc. R. Soc. Lond. Ser. A Math. Phys. Eng. Sci. 241 (1226) (1957) 376–396, http://dx.doi.org/10.1098/rspa.1957.0133.
[36] T. Mori, K. Tanaka, Average stress in matrix and average elastic energy of materials with misfitting inclusions, Acta Metall. 21 (5) (1973) 571–574, http://dx.doi.org/10.1016/0001-6160(73)90064-3.
[37] M.J. Abdolhosseini Qomi, F.J. Ulm, R.J.M. Pellenq, Physical origins of thermal properties of cement paste, Phys. Rev. Appl. 3 (6) (2015) 064010, http://dx.doi.org/10.1103/PhysRevApplied.3.064010.
[38] M. Zhdanov, Generalized effective-medium theory of induced polarization, Geophysics 73 (5) (2008) F197–F211, http://dx.doi.org/10.1190/1.2973462.
[39] D.A. Miranda, S.P. Corzo, C.G. Correa, Cervical cancer detection by electrical impedance in a Colombian setting, J. Phys. Conf. Ser. 434 (1) (2013) 012056, http://dx.doi.org/10.1088/1742-6596/434/1/012056.
[40] S. Vega, S. Corzo, D. Miranda, Sensibility analysis of the electrical impedance parameters by the Monte Carlo method, J. Phys. Conf. Ser. 1514 (1) (2020) 012001, http://dx.doi.org/10.1088/1742-6596/1514/1/012001.
[41] Roche, Triton X-100 product information, 2022, https://www.sigmaaldrich.com/deepweb/assets/sigmaaldrich/product/documents/235/712/11332481001bul.pdf, (accessed 13 June 2022).
[42] Sika, Datasheet SikaPlast-328, 2022, https://col.sika.com/dms/getdocument.get/0b5b4477-e5db-3db3-9629-a4360e060629/co-ht_SikaPlast%20328.pdf, (accessed 13 June 2022).
[43] Euclid-Group, Datasheet EUCON 37, 2022, http://12.156.76.244/media/1106/eucon-37.pdf, (accessed 13 June 2022).
[44] L.M. Echeverry-Cardona, N. Álzate, E. Restrepo-Parra, R. Ospina, J.H. Quintero-Orozco, Time-stability dispersion of MWCNTs for the improvement of mechanical properties of Portland cement specimens, Materials 13 (18) (2020) 4149, http://dx.doi.org/10.3390/ma13184149.
[45] ASTM Standard C 349-18: Standard Test Method for Compressive Strength of Hydraulic-Cement Mortars (Using Portions of Prisms Broken in Flexure), ASTM International, 2018, https://www.astm.org/c0349-18.html, (accessed 13 June 2022).
[46] S. Wen, D. Chung, The role of electronic and ionic conduction in the electrical conductivity of carbon fiber reinforced cement, Carbon 44 (11) (2006) 2130–2138, http://dx.doi.org/10.1016/j.carbon.2006.03.013.
[47] X. Chen, Y.F. Zhao, L.S. Wang, J. Li, Recent progresses of global minimum searches of nanoclusters with a constrained Basin-Hopping algorithm in the TGMin program, Comput. Theor. Chem. 1107 (2017) 57–65, http://dx.doi.org/10.1016/j.comptc.2016.12.028.
[48] D.A. Miranda, S.A. Jaimes, J.M. Bastidas, Assessment of carbon steel microbiologically induced corrosion by electrical impedance spectroscopy, J. Solid State Electrochem. 18 (2) (2014) 389–398, http://dx.doi.org/10.1007/s10008-013-2262-5.
[49] H. Cui, X. Yan, M. Monasterio, F. Xing, Effects of various surfactants on the dispersion of MWCNTs–OH in aqueous solution, Nanomaterials 7 (9) (2017) 262, http://dx.doi.org/10.3390/nano7090262.
[50] O. Mendoza, G. Sierra, J.I. Tobón, Influence of super plasticizer and $Ca(OH)_2$ on the stability of functionalized multi-walled carbon nanotubes dispersions for cement composites applications, Constr. Build. Mater. 47 (2013) 771–778, http://dx.doi.org/10.1016/j.conbuildmat.2013.05.100.
[51] M. Sharif Sh., F. Golestani Fard, E. Khatibi, H. Sarpoolaky, Dispersion and stability of carbon black nanoparticles, studied by ultraviolet–visible spectroscopy, J. Taiwan Inst. Chem. Eng. 40 (5) (2009) 524–527, http://dx.doi.org/10.1016/j.jtice.2009.03.006.
[52] Q. Li, J.S. Church, A. Kafi, M. Naebe, B.L. Fox, An improved understanding of the dispersion of multi-walled carbon nanotubes in non-aqueous solvents, J. Nanopart. Res. 16 (7) (2014) 1–12, http://dx.doi.org/10.1007/s11051-014-2513-0.
[53] A. Gaurav, K. Singh, Effect of pristine MWCNTs on the fatigue life of GFRP laminates-an experimental and statistical evaluation, Composites B 172 (2019) 83–96, http://dx.doi.org/10.1016/j.compositesb.2019.05.069.
[54] P.C. Ma, N.A. Siddiqui, G. Marom, J.K. Kim, Dispersion and functionalization of carbon nanotubes for polymer-based nanocomposites: A review, Composites A 41 (10) (2010) 1345–1367, http://dx.doi.org/10.1016/j.compositesa.2010.07.003.
[55] D. Lin, B. Xing, Adsorption of phenolic compounds by carbon nanotubes: role of aromaticity and substitution of hydroxyl groups, Environ. Sci. Technol. 42 (19) (2008) 7254–7259, http://dx.doi.org/10.1021/es801297u.
[56] L. Weiwen, et al., Electrochemical impedance interpretation for the fracture toughness of carbon nanotube/cement composites, Constr. Build. Mater. 114 (2016) 499–505, http://dx.doi.org/10.1016/j.conbuildmat.2016.03.215.
[57] E. García-Macías, R. Castro-Triguero, A. Sáez, Micromechanics modeling of nanomodified cement-based composites: Carbon nanotubes, in: Nanotechnology in Cement-Based Construction, Jenny Stanford Publishing, 2020, pp. 173–214, http://dx.doi.org/10.1201/9780429328497.
[58] V. Kumar, A. Rawal, Tuning the electrical percolation threshold of polymer nanocomposites with rod-like nanofillers, Polymer 97 (2016) 295–299, http://dx.doi.org/10.1016/j.polymer.2016.05.041.
[59] O.A. Mendoza Reales, P. Duda, R. Dias Toledo Filho, Effect of a carbon nanotube/surfactant aqueous dispersion on the rheological and mechanical properties of Portland cement pastes, J. Mater. Civ. Eng. 30 (10) (2018) 04018259, http://dx.doi.org/10.1061/(ASCE)MT.1943-5533.0002452.
[60] D. Green, The historical development of complex numbers, Math. Gazette 60 (412) (1976) 99–107, http://dx.doi.org/10.2307/3616235.